

# Stress Wave Tomography of Wood Internal Defects using Ellipse-Based Spatial Interpolation and Velocity Compensation

Xiaochen Du,<sup>a,b</sup> Shaozhe Li,<sup>b</sup> Guanghui Li,<sup>c</sup> Hailin Feng,<sup>c</sup> and Shengyong Chen<sup>a,\*</sup>

In this paper, a novel stress wave tomography method, using spatial interpolation and velocity compensation, is proposed for the detection of internal defects in wood, based on the measured time of flight data and the assumption that stress waves propagate in straight lines in the cross-sectional area of wood. First, an improved ellipse-based spatial interpolation method is proposed, which could be used to estimate the velocity value of a grid cell by the elliptic affected zones corresponding to the nearby velocity rays. Second, because of the anisotropic property of wood, a velocity compensation method was applied to obtain more accurate input data for spatial interpolation. Then, the internal graph of the cross-section of a wood trunk could be reconstructed by the proposed algorithm. Four wood samples, with different defects, were used to test the proposed tomography method in the experiment. The results showed that the proposed method performed well and was able to resist signal interference caused by the density variation of the defective area.

*Keywords:* Stress wave; Tomography; Wood internal defects; Spatial interpolation; Velocity compensation

*Contact information:* a: College of Computer Science, Zhejiang University of Technology, Hangzhou, China; b: School of Information Engineering, Zhejiang Agricultural and Forestry University, Hangzhou, China; c: Zhejiang Provincial Key Laboratory of Forestry Intelligent Monitoring and Information Technology, Hangzhou, China; \*Corresponding author: sy@ieee.org

## INTRODUCTION

Internal defects in wood are difficult to observe directly. They can endanger the tree's health and reduce the quality of the logs, so it is important to detect wood internal defects conveniently. The stress wave method is considered to be an appropriate technique for the detection of wood internal conditions. Different from other nondestructive techniques, the stress wave technique is low-cost, portable, and harmless (Reinprecht and Hibky 2011; Wessels *et al.* 2011; Brancheriau *et al.* 2012; Wang 2013).

Usually, stress wave velocity is the essential feature of detection. The propagation velocity of stress waves in defective wood is slower than in sound wood (Ross *et al.* 1998). Assuming that stress wave propagation in wood follows a straight path, the transmission time of a stress wave through the cross-section of wood can be measured. This fundamental signal is commonly called time of flight (TOF) (Li *et al.* 2012). Then, the single-ray velocity of a stress wave can be calculated, and it can be used to inspect the soundness of wood by measuring the velocity difference between the value and a reference value (Ross *et al.* 1994). Furthermore, once the multi-ray signals of a stress wave are measured, the horizontal distribution of the stress wave propagation velocity in wood can also be analyzed (Johnstone *et al.* 2010; Lin *et al.* 2011).

Tomikawa *et al.* (1986) inspected wooden poles using the tomography method. Since then, the straight-ray tomography has attracted more and more attention from many researchers. The travel time inversion algorithm for trunks was developed, and the cross-section of a cavity can be detected using acoustic wood tomography (Schubert *et al.* 2009). Ultrasonic computed tomography in reflection was used to assess the integrity of green wood, and qualitative reflectivity images were obtained by reflection tomography (Brancheriau *et al.* 2008). An image reconstruction method for detecting wood internal decay was proposed that uses an interpolation algorithm, which estimated the velocity values of the unknown grid cells based on the surrounding information (Feng *et al.* 2014).

Although stress wave tomography, based on TOF data, has been considered a useful detection method for wood internal defects, the quality of reconstructed images still can be improved. For example, the quality of images taken near the sensor is significantly lower than those taken in the middle part of a trunk using TOF and the tomography method (Gilbert and Smiley 2004). When an internal defect is present in the tree trunk, the acoustic tomography tends to overestimate its size (Wang *et al.* 2009). There have been investigations showing that tomographic images improved if the applied frequency was increased, if the number of sensors was higher, and if the applied algorithm was more advanced (Divos and Divos 2005). Therefore, more sophisticated tomography algorithm can be developed.

In addition to tomography algorithm, the input data also can be processed in order to get high quality reconstructed images. Experimental analysis of the acoustic anisotropy of wood has been presented, and the dependence between the propagation velocity of stress wave and the natural anisotropy axis in the cross-section has been discussed as well (Dikrallah *et al.* 2006). The stress wave velocity patterns in the cross-section of wood have been examined, and an analytical model of stress wave velocity and angle of propagation has been developed (Li *et al.* 2014). Therefore, the measured TOF data is different from that of other research field, such as guided wave TOF data that can be utilized directly for the detection of isotropic materials (Zeng *et al.* 2013). Input data in this application should be corrected before the process of straight-ray tomography.

This paper focuses on the high quality stress wave tomography of wood's internal defects by improving tomography algorithm, and calculating more accurate input data. Based on the measured TOF data for stress waves, along with the assumption that stress waves propagate in a straight line from the transmitter to the receiver in the cross-section of a wood trunk, a novel interpolation is proposed for the tomography, and it utilizes the original graph of velocity rays directly and abundantly. Additionally, more accurate input data for the interpolation is obtained based on the propagation characteristics of stress waves in the cross-section of wood. Consequently, after all the grid cells have been estimated by the proposed method, the internal graph of the cross-section of wood can be reconstructed. Four samples, with different defects, are used to test the proposed tomography method in the experiment. The compared results show the performance of the proposed method.

## EXPERIMENTAL

The device used to measure stress wave signals was developed at the Laboratory of Intelligent Measurement Technology at Zhejiang Agricultural and Forestry University.

As shown in Fig. 1, this device contains a stress wave signal processor box, 12 sensors, a hammer, and several data wires.



Fig. 1. Stress wave measurement device

As shown in Fig. 2(a), stress wave sensors were equally spaced around the cross-section of a trunk section using steel nails. After knocking any sensor using the steel hammer, stress waves were generated. When a sensor is knocked, the impulse energy is introduced into the trunk generating low frequency (less than 7 kHz mostly) and high energy stress waves. All remaining sensors will receive the stress wave signal. Then, the signal processor analyzes the signals with DSP technique in order to obtain the stress wave transmission time. Short-time energy and double threshold detection algorithm are used to estimate the propagation time, and the details were in our previous work (Fang *et al.* 2011). To achieve complete TOF data, it is necessary to knock each sensor one by one until the propagation time of the stress wave between any two sensors is obtained. The TOF data can be represented as follows,

$$T = \begin{bmatrix} t_{11} & t_{12} & \dots & t_{1N} \\ t_{21} & t_{22} & \dots & t_{2N} \\ \dots & \dots & \dots & \dots \\ t_{N1} & t_{N2} & \dots & t_{NN} \end{bmatrix} \quad (1)$$

where  $N$  is the total number of sensors (which is usually 12), and  $t_{ij}$  represents the propagation time from sensor number  $i$  to sensor number  $j$ .

On the other hand, the circumference and arc length between every two adjacent sensors can be measured using a tape measure on each sample based on the assumption that the cross-section of wood is of circular shape. This allows researchers to obtain the distance between any two sensors and garner geometric information of the cross-section from tomography. Therefore, the propagation velocity of the stress waves between any two sensors can also be calculated and represented as follows,

$$V = \begin{bmatrix} v_{11} & v_{12} & \dots & v_{1N} \\ v_{21} & v_{22} & \dots & v_{2N} \\ \dots & \dots & \dots & \dots \\ v_{N1} & v_{N2} & \dots & v_{NN} \end{bmatrix} = \begin{bmatrix} 0 & d_{12}/t_{12} & \dots & d_{1N}/t_{1N} \\ d_{21}/t_{21} & 0 & \dots & d_{2N}/t_{2N} \\ \dots & \dots & \dots & \dots \\ d_{N1}/t_{N1} & d_{N2}/t_{N2} & \dots & 0 \end{bmatrix} \quad (2)$$

where  $d_{ij}$  represents the measured distance between sensor number  $i$  and sensor number  $j$ .  $V$  can be used as the input for the straight-ray tomography method.

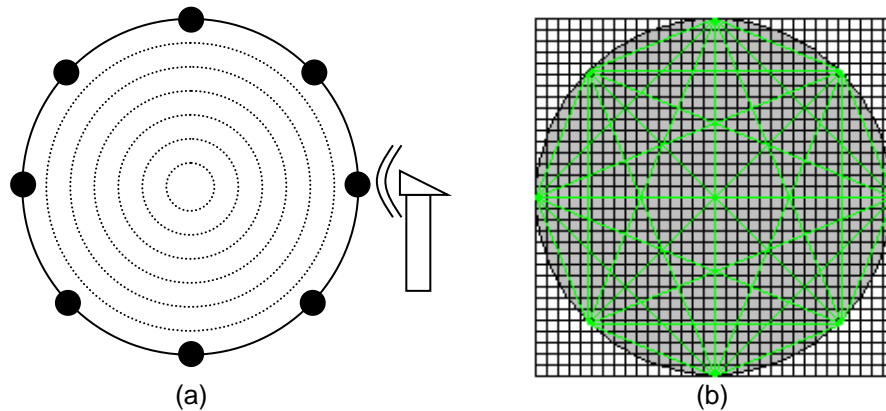


**Fig. 2.** (a) Diagram of measurement; (b) grid graph for tomography

### An Improved Ellipse-Based Spatial Interpolation Method

A grid graph was generated that depicted the cross-section of a wood trunk, as shown in Fig. 2(b). If the velocity value of each grid cell could be calculated accurately, grids will show a 2D image and a corresponding color based on the velocity value. The grid graph for the tomography of wood's internal structure can be seen as a matrix, which is usually sparse. Therefore, estimating the velocity values of every grid cell based on the velocity rays is the key problem.

Spatial interpolation is an effective way to reconstruct the image of wood's internal structure. Commonly, the inputs of spatial interpolation are several initial points, and the values of the unknown grid cells can be calculated using the values of the initial known grid cells, utilizing a certain interpolation method. To reconstruct a 2D image of internal tree decay, Feng *et al.* (2014) computed every intersection for each set of two velocity rays. Then, these intersections were used as the input for the interpolation method. However, the value of a certain intersection is the mean value of two rays in their work. This strategy lacks a solid theory, and their results did not show good performance. Actually, the values of all velocity rays are the original input for the tomography method in this application, so converting the input from lines to intersections will certainly cause error, no matter how one determines the value of a certain intersection.

Direct utilization of the values of the total velocity rays is another strategy. A spatial interpolation method for tomography using ellipses has been developed (Rose and Royer 2008; Zeng *et al.* 2013). As shown in Fig. 3(a), each ray affects the surrounding area (called affected zone) and the shape of affected zone is elliptical. Then, the value of the grid cells in affected zone is equal to the value of the corresponding ray. If a certain grid cell is in several affected zones simultaneously, the value of this grid cell will be equal to the mean value of those affected zones. In previous work, this spatial interpolation method was applied to guided wave tomography, which behaves similar to stress wave tomography in the process of interpolation, and the general location of structural damage was detected (Zeng *et al.* 2013).

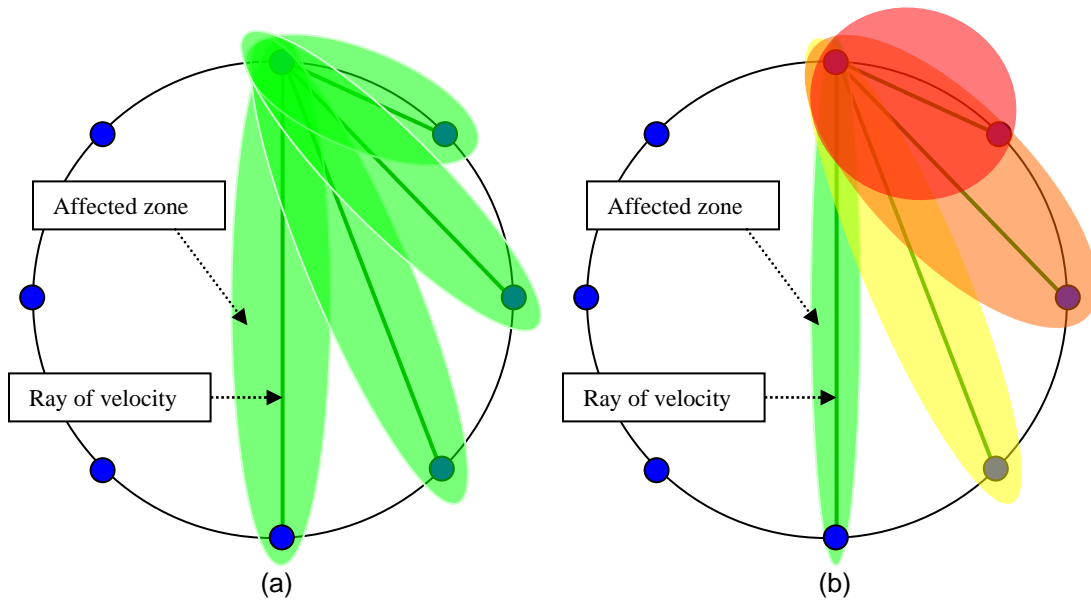


**Fig. 3.** (a) Illustration of spatial interpolation using a basic ellipse; (b) illustration of the improved method

A ray here represents the virtual propagation path of a stress wave, and its value represents the velocity value of stress wave. Obviously, there are internal defects present on the path if the value of a certain ray is low, but the exact location of the defective part is still uncertain. Ellipses with the same eccentricity will have a greater effect on the middle portion of a ray, but the defects may be near the sensor or somewhere else. Therefore, the spatial interpolation method that uses a basic ellipse can be improved. The length is another key property of the ray. The affected zones that corresponded to shorter rays are more likely to overlap with the defective region. As shown in Fig. 3(b), the area of the affected zone that corresponds to short rays should be larger, and the weight of the affected zone that corresponds to short rays should also be strengthened. The shape of the elliptic zone can be expressed as,

$$c = b / a \tag{3}$$

where  $a$  is the long axis of the ellipse and  $b$  is the short axis of the ellipse. Therefore,  $c$  is similar to the eccentricity, and the controlling coefficient for a certain ray can be given as,

$$c_{ij} = \begin{cases} 1 - [|j - i| / (N / 2)] & |j - i| < (N / 2) \\ 1 - [(N - |j - i|) / (N / 2)] & |j - i| > (N / 2) \\ 0.1 & |j - i| = (N / 2) \end{cases} \tag{4}$$

where:  $i \in [1, N]$  is the sensor number of a transmitter,  $j \in [1, N]$  is the sensor number of a receiver,  $N$  is the total number of sensors, and  $c_{ij}$  represents the ray from sensor number  $i$  to sensor number  $j$ . The value of  $a_{ij}$  is known, so the shape of each affected zone can be controlled by  $b_{ij}$ :

$$b_{ij} = c_{ij} \times a_{ij} \tag{5}$$

Then, whether a certain grid cell is affected by a certain elliptic zone can be identified as follows,

$$h(x, y) = \begin{cases} 1 & D_{xb}^2 / a^2 + D_{ya}^2 / b^2 \leq 1 \\ 0 & D_{xb}^2 / a^2 + D_{ya}^2 / b^2 > 1 \end{cases} \quad (6)$$

where  $D_{xb}$  is the distance between a certain grid cell and the short axis of a certain ellipse, and  $D_{ya}$  is the distance between a certain grid cell and the long axis of a certain ellipse. If  $h(x, y) = 1$ , it means that the grid cell is affected by a certain ellipse.

Additionally, when a certain grid cell is affected by more than one elliptic zone, all these elliptic zones and their corresponding rays can be recorded. Then, the velocity value of the grid cell can be calculated as,

$$v_{xy} = \sum_{k=1}^m w_k \times v_k \quad (7)$$

where  $v_{xy}$  is the estimated velocity value of a certain grid cell,  $v_k$  is the velocity value of a certain ray that affects the specific grid cell,  $w_k$  is weighting coefficient, and  $m$  is the total number of rays that affect the specific grid cell, simultaneously. Considering that elliptical zones that correspond to short rays should weigh more,  $w_k$  can be given as,

$$w_k = (1/l_k) / \sum_{z=1}^m (1/l_z) \quad (8)$$

where  $l_z$  is the length of a certain ray.

### Velocity Compensation of Stress Wave

Anisotropy is an important property of wood. Accordingly, the stress wave TOF data in the cross-section of wood have their own characteristics. As shown in Fig. 4, the stress wave velocity pattern in the cross-section of sound wood is revealed directly using 2D visualization. Figure 4(a) shows the cross-section of a sound wood trunk, and the expected graph of velocity rays, based on measured TOF data, is shown in Fig. 4(b). However, the velocity values are not completely equal, because of the anisotropy of wood, and the real graph of the velocity rays is shown in Fig. 4(c).

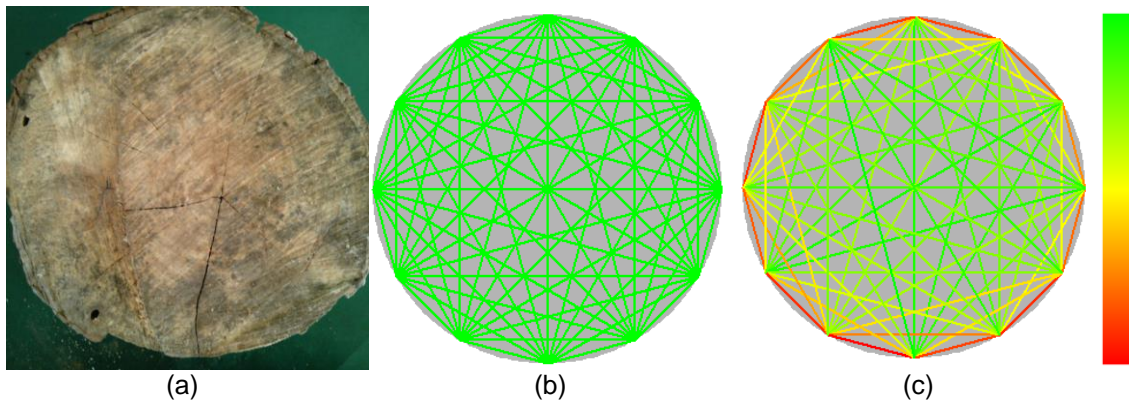


**Fig. 4.** (a) Photograph of the cross-section of a sound sample; (b) expected graph of velocity rays; (c) real graph of velocity rays

The color red represents low velocity, and green represents high velocity. Obviously, the real graph of the velocity rays should be corrected to make it more similar to the expected diagram, before the process of interpolation.

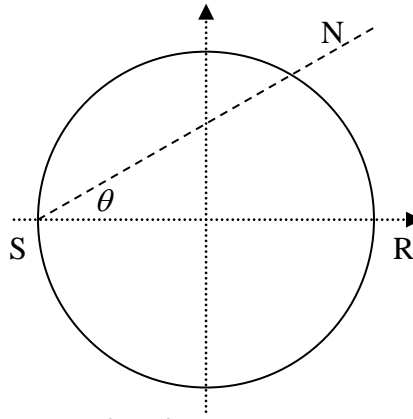


**Fig. 5.** Coordinate system of cross-section plane

The stress wave velocity between two sensors is related to the angle between the pair of sensors. The relationship between the stress wave velocity  $v$  and the angle  $\theta$  in Fig. 5 can be given as follows (Dikrallah *et al.* 2006):

$$v_N = v_R \cos^2(\theta) \sqrt{1 + \frac{E_T}{E_R} \tan^4(\theta) + 2 \frac{G_{RT}}{E_R} \tan^2(\theta)} \quad (9)$$

where  $v_N$  is the non-radial velocity,  $v_R$  is the radial velocity,  $\theta$  is the angle between them,  $E_R$  is the radial modulus of elasticity,  $E_T$  is the tangential modulus of elasticity, and  $G_{RT}$  is shear modulus.  $E_R$ ,  $E_T$ , and  $G_{RT}$  are constants. Equation 9 can be simplified (Li *et al.* 2014). If  $f(\theta)$  represents the ratio of  $v_N$  to  $v_R$ , then

$$f(\theta) = \cos^2(\theta) \sqrt{g(\theta)} \quad (10)$$

where,

$$g(\theta) = \sqrt{1 + \frac{E_T}{E_R} \tan^4(\theta) + 2 \frac{G_{RT}}{E_R} \tan^2(\theta)} \quad (11)$$

Therefore,  $f(\theta)$  can be expanded to a Taylor series at  $\theta = 0$  as follows:

$$\begin{aligned} f(\theta) &= f(0) + \frac{1}{1!} f'(0)\theta + \frac{1}{2!} f''(0)\theta^2 + O(\theta^3) = 1 - (1 - \frac{G_{RT}}{E_R})\theta^2 + O(\theta^3) \\ &\approx -(1 - \frac{G_{RT}}{E_R})\theta^2 + 1 \end{aligned} \quad (12)$$

Although  $\alpha = -(1 - G_{RT} / E_R)$  should be determined by the mechanical properties of wood trunk,  $\alpha \approx -0.2$  was estimated based on real test data (Li *et al.* 2014). The relationship between  $v_N$  and  $v_R$  can be simplified as follows:

$$v_N = (-0.2\theta + 1)v_R \quad (13)$$

To obtain more accurate input data for the proposed spatial interpolation method, based on Eq.13, the velocity value of each non-radial wave path can be compensated as follows,

$$v'_N = v_N / (-0.2\theta + 1) \quad (14)$$

where  $v_N$  is the original velocity value of a certain non-radial wave path, and  $v'_N$  is the velocity value of a certain non-radial wave path after compensation.

Finally, the improved tomography method of detecting wood internal defects using ellipse-based spatial interpolation and velocity compensation is proposed, and the specific process of the algorithm is as follows:

Step 1. Initialization. (Generating grid graph, calculating all values of velocity rays with Eq. 2, and normalizing them.)

Step 2. Compensating the values of all non-radial velocity rays with Eq. 14.

Step 3. Generating all of the affected zones with Eq. 4 and Eq. 5.

Step 4. For a certain grid cell, one can record all of the elliptic zones that affect it with Eq. 6, and calculate its velocity value, using Eq. 7 and Eq. 8.

Step 5. Repeating Step 4 until every grid cell has been processed.

Step 6. Visualization (reconstructing the 2D image with a certain color scale).

Four typical wood samples were selected to test the proposed method. For each sample, 12 sensors were used. Velocity measurements of the stress waves for each sample were repeated several times to make certain stable TOF data were obtained. To express the appropriate visual effects for the tomography, a three-color scheme was used to represent the internal conditions of the samples using RGB values. Green (RGB(0,255,0)) shows the maximum value of velocity ray, Yellow (RGB(255,255,0)) shows the median, and Red (RGB(255,0,0)) shows the minimum. The color range was between Green and Red, and all values of velocity rays are distributed in this range evenly. Therefore, Green represents high stress wave velocity, high density, and sound wood. Yellow represents low stress wave, relatively low density, and potentially defective wood. Red represents the lowest stress wave velocity, lowest density, and defects.

## RESULTS AND DISCUSSION

A picture of the first sample with large defects is shown in Fig. 6(a). It can be seen that hollow defects were present in the bottom-left area of the cross-section. The diameter of this sample was 36 cm, and the diameter of the defective area was about 19 cm. The original graph for the velocity rays is shown in Fig. 6(b). This graph is the visualization of all velocity rays, which is dependant on the measured propagation time and distance. As stated before, those rays passing through the defective regions are relatively red (low value), and those rays passing though healthy regions are relatively green (high value). The corrected graph for the velocity rays is shown in Fig. 6(c). To demonstrate the performance of the proposed method, this study repeated the methods proposed by Feng *et al.* (2014) and Zeng *et al.* (2013). The same samples, corrected input data, and color scale were used during testing.

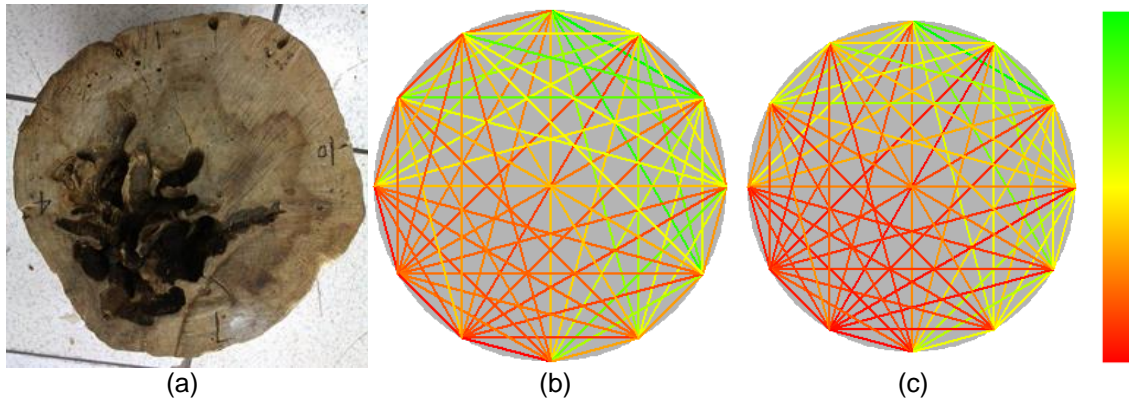


**Fig. 6.** (a) sample 1; (b) graph of original velocity rays; (c) graph of compensated velocity rays

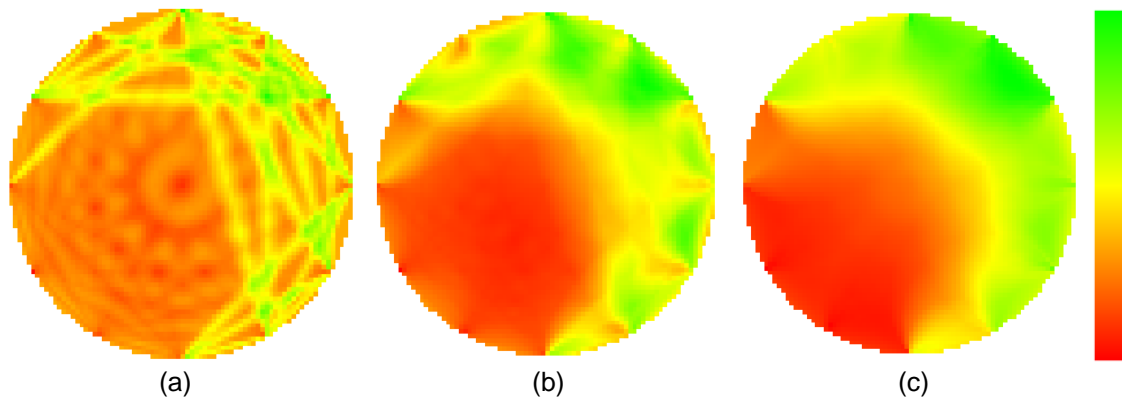


**Fig. 7.** (a) Feng's result; (b) Zeng's result; (c) tomography result of proposed method

The tomography comparison results are shown in Fig. 7 (a), (b), and (c). Only the approximate location of defects was determined by Feng's method, and the shape of defects was very different from the real defective shape. Even worse, some healthy regions were incorrectly detected as defects. The location and shape of the internal defects were detected by Zeng's method. However, some healthy areas, especially those near the sensors, were incorrectly detected as defects. The location and shape of wood internal defects were detected by proposed method. Additionally, areas near sensors were also detected correctly, and the tomography result was quite similar to the real photograph.

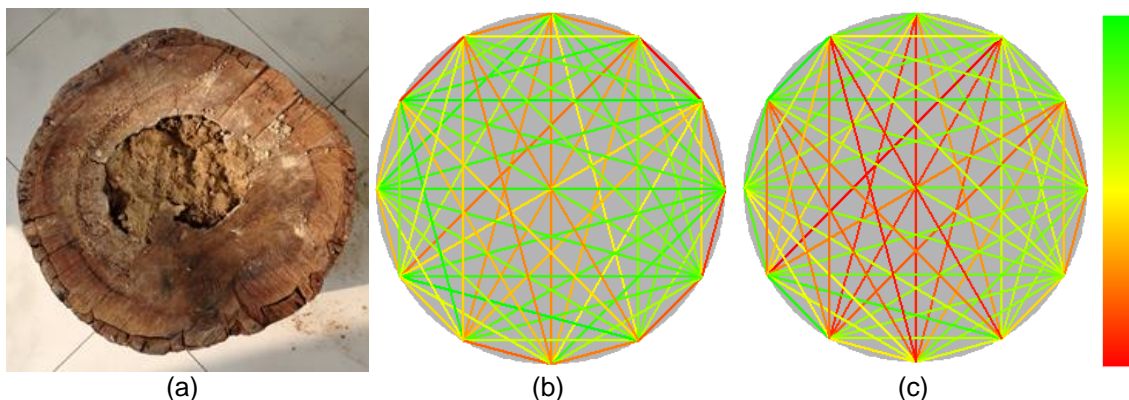


**Fig. 8.** (a) sample 2; (b) graph of original velocity rays; (c) graph of compensated velocity rays

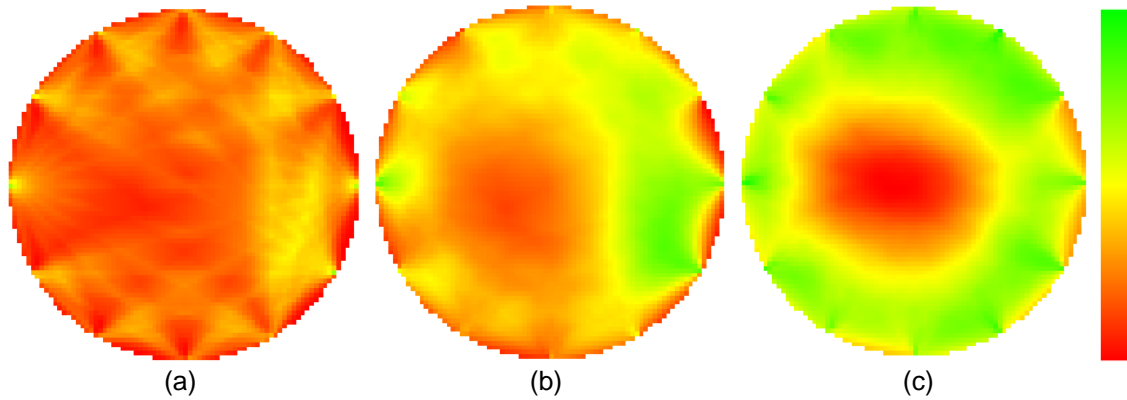


**Fig. 9.** (a) Feng's result; (b) Zeng's result; (c) tomography result of proposed method

The second sample is shown in Fig. 8(a). There are hollow defects in the middle area of the cross-section. The diameter of this sample is 33 cm, and the diameter of the defective area is about 11 cm. To test the ability to resist signal interference during tomography, some clay was filled in the hole, so the density of the middle area of the cross-section was changed. Then, the transmission velocity difference between sound wood and defects would weaken. It increased difficulty for tomography because of this artificial arrangement, and the original velocity ray graph is shown in Fig. 8(b). Many rays passing through the defective regions were not relatively red, although they were expected to be red rays. The corrected graph of the velocity rays is shown in Fig. 8(c). Some rays that cross through defective regions correctly turned from orange to red, such as the path from most bottom sensor to most top sensor. However, it can be observed that there were still some green rays crossing through defective areas due to signal interference, although they should be red, such as the path from the left-most sensor to the right-most sensor.

The tomography comparison results are shown in Fig. 9 (a), (b), and (c). Feng's method did not work in this pattern of input, and the tomography algorithm failed. Only the approximate location of the defective regions was detected by Zeng's method. Some healthy areas, especially those near sensors, were still incorrectly detected as defects. The location and shape of wood internal defects were once again detected by the proposed method. Additionally, areas near the sensors were detected correctly, and the tomography result was still quite similar to the real photograph.

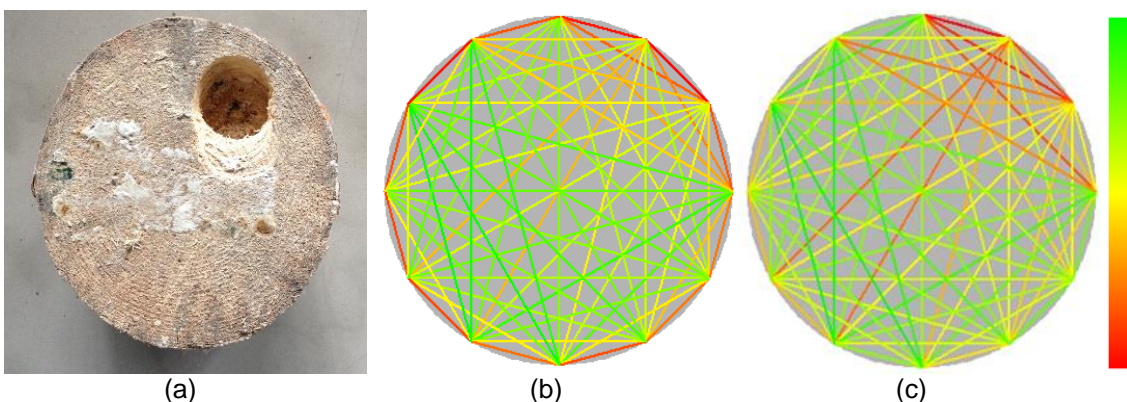


**Fig. 10.** (a) sample 3; (b) graph of original velocity rays; (c) graph of compensated velocity rays

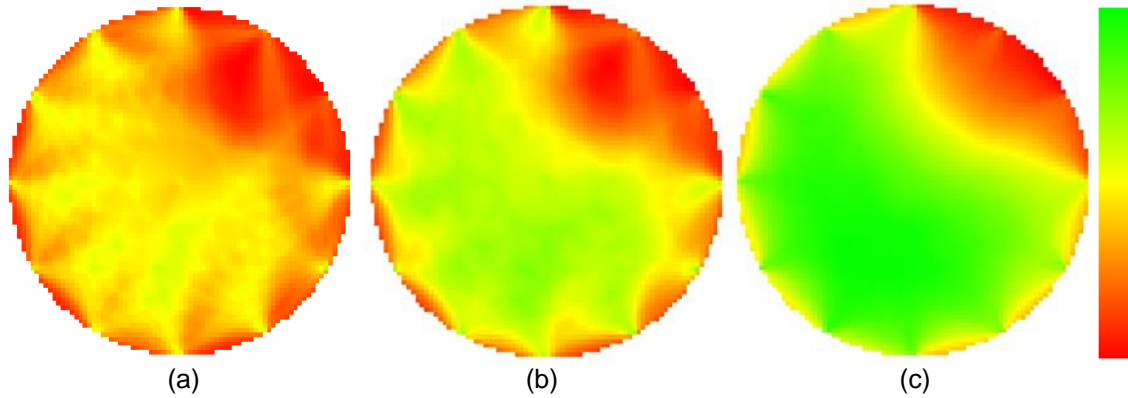


**Fig. 11.** (a) Feng's result; (b) Zeng's result; (c) tomography result of proposed method

The picture of the third sample with small defects is shown in Fig. 10(a). A small hole was made manually. The diameter of this sample was 23 cm, and the diameter of the hole was 5 cm. The original velocity ray graph is shown in Fig. 10(b). Many red rays were detected near the sensors because of the small defective region and the anisotropic property of wood, although they were expected to be green rays. The corrected graph of the velocity rays is shown in Fig. 10(c). Many rays near the sensors turned green or yellow; such results will benefit the subsequent interpolation.

The tomography comparison results are shown in Fig. 11 (a), (b), and (c). The approximate location of defects was determined with difficulty by Feng's method. But the area of detected defects was too large, and a lot of healthy regions were incorrectly detected as defects. The approximate location of the defective regions was detected, and healthy areas near sensors were still incorrectly detected as defects by Zeng's method. Additionally, the area of detected defects was larger than the area of real defects. The location of wood internal defects was detected, and the areas near sensors were still correctly detected as sound wood by proposed method. However, like other two methods, the area of detected defects was larger than the area of real defects.

The picture of the fourth sample with two separate defects is shown in Fig. 12(a). Two holes were made manually. One artificial hole was made on the top of the cross-section of the sample, and the other hole was on the bottom. The diameter of this sample was 24 cm, the diameter of the upper hole was 8 cm, and the diameter of the lower hole was 7 cm. The original velocity ray graph is shown in Fig. 12(b), and there was not an obvious pattern in the graph.

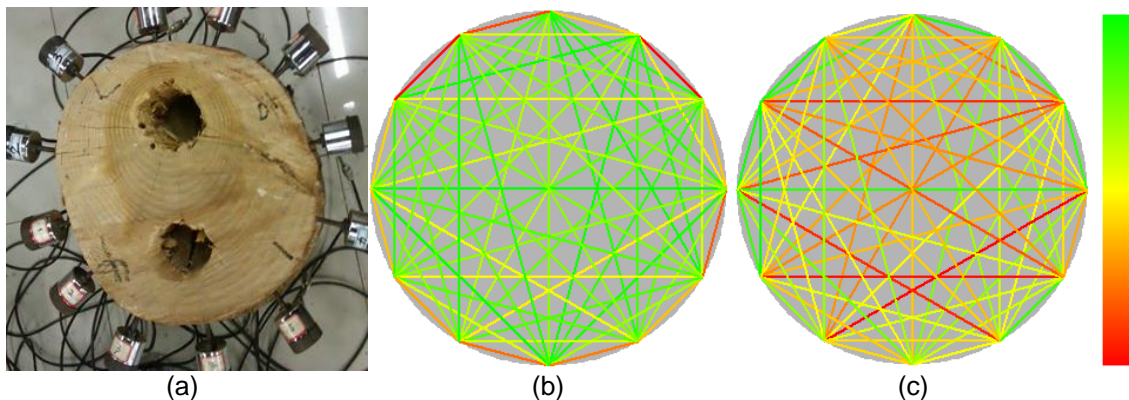


**Fig. 12.** (a) sample 4; (b) graph of original velocity rays; (c) graph of compensated velocity rays

The graph of the velocity rays after compensation is shown in Fig. 12(c). Almost all rays near the sensors turned green, and some rays crossing through defective regions turned from yellow to red.

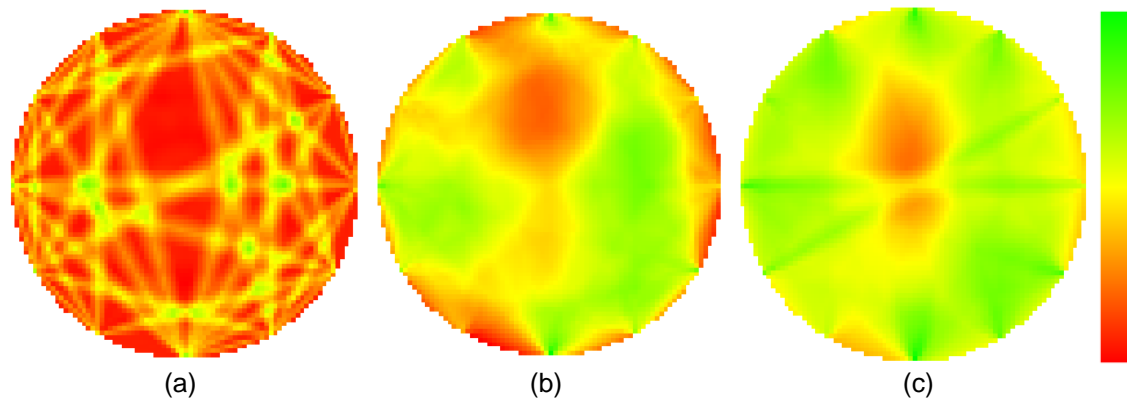


**Fig. 13.** (a) Feng's result; (b) Zeng's result; (c) tomography result of proposed method

The tomography comparison results are shown in Fig. 13 (a), (b), and (c). Feng's method failed again. The approximate locations of two defective areas were detected by Zeng's method. However, unfortunately, these two hollow regions joined together. Again, some healthy areas near the sensors were incorrectly detected as defects. Two separate holes were detected by the proposed method. It can be observed that the two defective areas are separate, and the upper hole is slightly larger than the lower hole. However, the location of the hollow defect below had not been detected accurately, so the distance between the two holes was shorter than in the real image.

Overall, the comparison of the original velocity rays graph and the compensated velocity rays graph shows that the velocity compensation method in this paper is effective. Defects in the first sample were the simplest, because a large number of red rays gathered in the bottom-left area of the cross-section. So it seems that there were not much differences between the two graphs. However, the red rays become denser in the bottom-left area of the cross-section after compensation, and this positive change is conducive to the following interpolation. Many rays that cross through defective regions turn from orange to red, and many rays near the sensors turn from red to green or yellow correctly due to velocity compensation in second and third experiments. Hence, the features of defects become obvious. For the fourth sample, the corrected graph helps to show the potential defect patterns. Therefore, velocity compensation is necessary to obtain more accurate input data for spatial interpolation, especially for complicated defects.

The comparison of the tomography results shows that Feng's method can only detect an approximate location of simple defects. In the first experiment, there was an abundance of red rays in the bottom-left area of the cross-section; therefore, there were certainly many red intersections in this area. Thus, the grid cells near these intersections became red according to their algorithm, and the approximate location of defects could be detected. However, there were differently colored rays in other areas (such as the top-right area), resulting in the appearance of a number of intersections with different colors, and the grid cells near these intersections will be different colors, despite the fact that they should be green. More errors occurred eventually. When processing complicated defects, such as the second and fourth samples, their algorithm failed. The reason is that

there were no longer dense red rays in a particular area. Overall, this method did not work well for it is dependent on simple graph of velocity rays, and the visual effect of tomography result is not as good as the other two methods.

The comparison of the tomography results also shows that Zeng's method can detect an approximate location of every sample. But their method cannot process regions near the sensors well. This occurs because there are inevitably many rays with different colors near a certain sensor in healthy area. The region nearest the sensors will be equally affected by the many elliptic zones according to their algorithm. Thus, the grid cells near this sensor will be orange, or even red, though they should be green or yellow. In general, equal shape and weight of affected zones led to poor visual experiences near the sensors, and the failed tomography near sensors can be seen as the common fault of their method.

The proposed method shows the best performance based on the comparison of the tomography results. When processing simple defects, such as the first sample, the location and shape of wood internal defects were detected correctly, and the regions near sensors were also detected correctly. Although there are inevitably many rays with different colors near a certain sensor in a healthy area, the length of each ray is different. It can be seen that red rays are long and green rays are relatively short near a certain sensor in a healthy area. Thus, green rays weigh more and affect a wider area, according to the proposed algorithm. Consequently, areas near sensors in healthy zones were detected as sound wood (green). When processing a sample with artificial signal errors, such as the second sample, the green rays near every sensor are relatively short, so they are more affected than the red or yellow rays. Therefore, the areas near the sensors in healthy zones were once again detected as sound wood, and the proposed algorithm can resist signal interference caused by the density variation of defective area. When processing complicated defects, such as the third and fourth samples, the location of wood internal defects can still be detected, and the areas near sensors can also be correctly detected as sound wood. However, the tomography results are not as good as detecting simple defects. The reasons for the results are measurement errors caused by the anisotropy of wood with complicated defects, as well as the limited number of sensors and the limitation of the algorithm processing the complex defects.

## CONCLUSIONS

1. The experimental results show that the improved spatial interpolation method performs better than spatial interpolation using basic ellipses, especially when processing the regions near the sensors.
2. The second experiment shows that the proposed spatial interpolation method can resist signal interference caused by the density variation of defective area.
3. The third and fourth experiments show that the proposed spatial interpolation method can detect complicated defects, such as two separated defects and small defects; however, the tomography results are not as good at detecting simple defects.
4. Because of the anisotropic property of wood, velocity compensation is necessary when conducting a stress wave tomography to obtain more accurate input data for spatial interpolation.

## ACKNOWLEDGMENTS

The authors are grateful for the support of the Natural Science Foundation of China (Grant. No. 61272313, 61325019, and 61472368), the Natural Science Foundation of Zhejiang Province, China (Grant. No. LQ13F020013 and LY15F020034), the Science and Technology Department of Zhejiang Province, China (Grant. No. 2014C31044), and the Key Laboratory of Forestry Intelligent Monitoring and Information Technology Research of Zhejiang Province, China (Grant. No. 100151402).

## REFERENCES CITED

- Brancheriau, L., Lasaygues, P., Debieu, E., and Lefebvre, J. P. (2008). "Ultrasonic tomography of green wood using a non-parametric imaging algorithm with reflected waves," *Annals of Forest Science* 65(7), 712-718. DOI: 10.1051/forest:200851
- Brancheriau, L., Ghodrati, A., Gallet, P., Thauay, P., and Lasaygues, P. (2012). "Application of ultrasonic tomography to characterize the mechanical state of standing trees (*Picea abies*)," *Journal of Physics: Conference Series* 353, 012007. DOI: 10.1088/1742-6596/353/1/012007
- Dikrallah, A., Hakam, A., Kabouchi, B., Brancheriau, L., Bailleres, H., Famiri, A., and Ziani, M. (2006). "Experimental analysis of acoustic anisotropy of green wood by using guided waves," *Proceedings of the ESWM-COST Action E35*, Florence, Italy, pp. 149-154.
- Divos, F., and Divos, P. (2005). "Resolution of stress wave based acoustic tomography," *14<sup>th</sup> International Symposium on Nondestructive Testing of Wood*, Hannover, Germany, pp. 309-314.
- Fang, Y., Feng, H., Li J., and Li G. (2011). "A DSP based stress wave instrument for wood decay detection," *International Journal of Digital Content Technology and its Applications* 5(8), 415-422. DOI: doi:10.4156/jdcta.vol5.issue8.48
- Feng, H., Li, G., Fu, S., and Wang, X. (2014). "Tomographic image reconstruction using an interpolation method for tree decay detection," *BioResources* 9(2), 3248-3263. DOI: 10.15376/biores.9.2.3248-3263
- Gilbert, E., and Smiley, E. (2004). "Picus sonic tomography for the quantification of decay in white oak (*Quercus alba*) and hickory (*Carya* spp.)," *Journal of the Arboriculture* 30(5), 277-281.
- Johnstone, D., Moore, G., and Tausz, M. (2010). "The measurement of wood decay in landscape trees," *Arboriculture & Urban Forestry* 36(3), 121-127.
- Li, L., Wang, X., Wang, L., and Allison, R. B. (2012). "Acoustic tomography in relation to 2D ultrasonic velocity and hardness mappings," *Wood Science and Technology* 46(1), 551-561. DOI: 10.1007/s00226-011-0426-y
- Li, G., Wang, X., Feng, H., Wiedenbeck, J., and Ross, R. J. (2014). "Analysis of wave velocity patterns in black cherry trees and its effect on internal decay detection," *Computers and Electronics in Agriculture* 104, 32-39. DOI: 10.1016/j.compag.2014.03.008
- Lin, C. J., Chang, T. T., Juan, M. Y., Lin, T. T., Tseng, C. L., Wang, Y. N., and Tsai, M. Y. (2011). "Stress wave tomography for the quantification of artificial hole detection in camphor tree (*Cinnamomum camphora*)," *Taiwan Journal of Forest Science* 26(1), 17-32.

- Reinprecht, L., and Hibky, M. (2011). "The type and degree of decay in spruce wood analyzed by the ultrasonic method in three anatomical directions," *BioResources* 6(4), 4953-4968. DOI: 10.15376/biores.6.4.4953-4968
- Rose, J. L., and Royer Jr., R. L. (2008). "A guided wave health monitoring approach for civil structures," *IMAC-XXVI: Conference & Exposition on Structural Dynamics*.
- Ross, R. J., Ward, J. C., and Tenwolde, A. (1994). "Stress wave nondestructive evaluation of wetwood," *Forest Products Journal* 44(7), 79-83.
- Ross, R. J., Brashaw, B. K., and Pellerin, R. F. (1998). "Nondestructive evaluation of wood," *Forest Products Journal* 48(1), 14-19.
- Schubert, S., Gsell, D., Dual, J., Motavalli, M., and Niemz, P. (2009). "Acoustic wood tomography on trees and the challenge of wood heterogeneity," *Holzforschung* 63(1), 107-112. DOI: 10.1515/HF.2009.028
- Tomikawa, Y., Iwase, Y., Arita, K., and Yamada, H. (1986). "Nondestructive inspection of a wooden pole using ultrasonic computed-tomography," *IEEE Transactions on Ultrasonics Ferroelectrics and Frequency Control* 33(4), 354-358. DOI: 10.1109/T-UFFC.1986.26842
- Wang, X., Wiedenbeck, J., and Liang, S. (2009). "Acoustic tomography for decay detection in black cherry trees," *Wood and Fiber Science* 41(2), 127-137.
- Wang, X. (2013). "Acoustic measurements on trees and logs: A review and analysis," *Wood Science and Technology* 47(5), 965-975. DOI: 10.1007/s00226-013-0552-9
- Wessels, C. B., Malan, F. S., and Rypstra, T. (2011). "A review of measurement methods used on standing trees for the prediction of some mechanical properties of timber," *European Journal of Forest Research* 130(6), 881-893. DOI: 10.1007/s10342-011-0484-6
- Zeng, L., Lin, J., Hua, J., and Shi, W. (2013). "Interference resisting design for guided wave tomography," *Smart Materials and Structures* 22(5), 1-12. DOI: 10.1088/0964-1726/22/5/055017

Article submitted: February 24, 2015; Peer review completed: April 20, 2015; Revised version received and accepted: May 7, 2015; Published: May 13, 2015.

DOI: 10.15376/biores.10.3.3948-3962